Korean J. Chem. Eng., 37(9), 1573-1584 (2020)
DOI: 10.1007/s11814-020-0554-x

pISSN: 0256-1115
eISSN: 1975-7220

Porous nano-hydroxyapatites doped into substrate for thin film composite forward osmosis membrane to show high performance

Weiwen Wang, Yue Guo, Miyu Liu, Xiaokun Song, and Jihai Duan†

State Key Laboratory of Ecochemical Industry, School of Chemical Engineering,
Qingdao University of Science and Technology, Qingdao 266042
(*Received 24 December 2019 • Resived 31 March 2020 • Accepted 4 April 2020*)

Abstract−The incorporation of inorganic nanoparticles into thin film composite forward osmosis (TFC FO) membranes is an effective method to alleviate internal concentration polarization (ICP) and enhance the flux performance of the FO membrane. In this paper, synthetic hydrophilic rod-like porous nano-hydroxyapatites (PNHAs) were doped into polysulfone (PSf) casting solution to form support layer by phase inversion; further interfacial polymerization was carried out to prepare a high performance TFC FO membrane. The results showed that the incorporation of PNHAs not only improved the thickness, porosity, hydrophilicity, and connectivity of the support layer, but also enhanced the roughness of the active layer. The measured mass transfer parameters prove that these improvements were beneficial. Further FO experiments showed that when using deionized water as the feed solution and 1 mol/L NaCl as the draw solution, TFN 0.75 showed higher water flux than TFC FO membrane in both AL-FS (18.5 vs 7.16 L/m^2·h) and AL-DS (33.26 vs 9.93 L/m^2·h) modes. Reverse salt flux had not increased significantly. At the same time, TFN 0.75 (697 μm vs 1,960 μm) showed the smallest structural parameter. This study shows that PNHA is a suitable nanomaterial for mitigating the ICP effect of FO membranes.

Keywords: Forward Osmosis, Nano-hydroxyapatites, Thin Film Nanocomposite Membrane, Desalination, Internal Concentration Polarization

INTRODUCTION

With one quarter of the world's population facing water shortages, it is imperative to seek methods for seawater desalination and wastewater treatment to obtain freshwater resources. Membrane separation technologies, such as ultrafiltration (UF), nanofiltration (NF), and reverse osmosis (RO), are more mature water treatment technologies on the market [1]. However, the high energy consumption, high fouling tendency and low membrane life brought by pressure driven approaches have become the main shortcomings of this technology, which are more prominent in the RO process [2-5].

Forward osmosis (FO) process uses the osmotic pressure difference between the solution on both sides of the membrane as the driving force, so the water spontaneous substrate passes through the semipermeable membrane from the feed solution (FS) with low osmotic pressure to the draw solution (DS) with high osmotic pressure [6]. Theoretically, the DS used in the FO process generates much higher osmotic pressure than hydraulics, which makes the FO membrane have higher flux performance. At the same time, the FO technology has low fouling propensity and high membrane life [7]. Complete FO technology includes FO and DS regeneration process, so it is not a true low-energy process and cannot replace RO at this stage. However, it can replace RO to take advantage of it in various desalination processes, such as using low-cost thermal energy sources or green energy for seawater desalination to reduce the cost, separation of FS with high fouling potential and high salinity [8-10].

However, before practical application in water treatment, the further development and commercialization of FO technology is hampered by the lack of efficient and stable FO membranes. The common FO membrane is thin film composite (TFC) FO membrane composed of a supporting layer (otherwise known as the substrate) and an active layer (AL) [11]. In this paper we decided to optimize the substrate. The ideal TFC FO membrane substrate has the following characteristics: (1) thin, porous, and low pore tortuosity [12]. Internal concentration polarization (ICP), which occurs inside the substrate, is caused by the change of solute concentration in the boundary layer in the substrate. ICP is the key factor limiting the flux of FO membrane, making the water flux much lower than the theoretical value [13]. The structural parameter (S) is used to measure ICP (equivalent to thickness×tortuosity/porosity). The thinner the substrate, the lower the tortuosity; the higher the porosity, the smaller the ICP effect is [14]. (2) Hydrophilicity. The hydrophilicity of the substrate is strongly positively correlated with the water permeability of the membrane. In addition, the hydrophilic substrate contributes to the well formation of the AL [15-17].

To obtain an FO membrane with better performance, researchers optimized the substrate based on the aforementioned characteristics. Including changing the physical structure of substrate such as electrospinning [18-21], changing the chemical properties of substrate (such as coating, grafting, polymer blending [22-25]). But more research has focused on dispersing the inorganic nanomaterials in the organic polymer substrates [26].

In recent years, researchers have incorporated zero-dimensional nanomaterials (such as zeolite [27], nano-$CaCO_3$ [28], Ag nano-

†To whom correspondence should be addressed.
E-mail: duanjihai@qust.edu.cn

particles [29], SiO_2 nanoparticles [30], TiO_2 nanoparticles [31]), one-dimensional nanomaterials (carbon nanotubes [32], halloysite nanotubes [33], ZnO nanorods [34]), two-dimensional nanomaterials (graphene oxide [35]) and their modified materials [36] into the substrate, which have brought significant improvements to the substrate structure and performance. Nanomaterials doped into the substrate mostly have these characteristics: nanometer size, high specific surface area, or hydrophilic, or porous. These characteristics alleviate the ICP, improve the structure of the substrate and the AL, and ultimately enhance the permeability and mechanical strength.

As mentioned, we believe that hydrophilic porous nanomaterials will have a beneficial effect on the membrane and are good candidates for modifying TFC membrane substrate [37]. We turned our attention to hydroxyapatite (HA), a weakly basic calcium phosphate with a molecular formula of $Ca_{10}(PO_4)_6(OH)_2$, which is mostly spherical or rod-shaped with a nanometer size of 50 to 200 nm. We added a template during the synthesis of HA to introduce a porous structure to prepare porous nanohydroxyapatites (PNHAs). As a novel polymer nanodoping material, the method of synthesizing PNHAs is simple, low-cost and eco-friendly [38]. It is worth emphasizing that the presence of hydroxyl groups enhances the dispersibility of PNHAs in casting solution and the hydrophilicity of the substrate. The existence of porous structure can increase the effective porosity and provide additional water pathways in the substrate. These physical and chemical properties are the key factors in the use of PNHAs to modify TFC FO membrane to realize their enormous potential in the water recovery process.

We prepared PNHAs powder by hydrothermal method and incorporated it into TFC FO membrane substrate to prepare a new thin film nano-composite (TFN) FO membrane. We studied the influence of different doping amounts of PNHAs on membrane structure and performance, especially on the permeability of the membrane. Under the premise that the salt permeability will not change significantly, our goal was to improve the membrane structure and water permeability. To our knowledge, this is the first time that incorporates PNHAs into TFC FO membranes to study its effect on the working mechanism of membrane, and we believe that this work is meaningful for desalination processes such as seawater desalination.

EXPERIMENTAL

1. Materials

The substrate was prepared by polysulfone particles (PSf, P-3500, Solvay), N,N-dimethylacetamide (DMAc, >99.5%), polyethylene glycol 400 (PEG 400). The aqueous phase monomer 1,3-phenylenediamine (MPD, >99%, Macklin), sodium dodecyl sulfate (SDS, Macklin) and organic phase monomers 1,3,5 -benzenetricarboxylic acid chloride (TMC, >98%, Macklin) dissolved in n-hexane were used to prepare polyamide (PA) AL. PNHAs powder was prepared by using calcium chloride ($CaCl_2$), disodium hydrogen phosphate (Na_2HPO_4), cetyltrimethylammonium bromide (CTAB), sodium hydroxide (NaOH), and ethanol. Membrane performance evaluation was performed using sodium chloride (NaCl). All unlabeled materials were analytical reagent, and the unlabeled materials were all from Sinopharm Chemical Reagent Co., Ltd. (China).

2. Preparation of PNHAs Powder

PNHAs powder was prepared according to previous substrate reported methods [39]. First, 0.5 mol/L $CaCl_2$ solution and Na_2HPO_4 solution were prepared separately. CTAB was added to Na_2HPO_4 solution at a ratio of n (CTAB)/n (PO_4^{3-}) of 1 and stirred for 1 h. The mixed solution was then substrately added to the strongly stirred $CaCl_2$ solution with the ratio of Ca^{2+}/PO_4^{3-} is 1.67, and the pH of the reaction system was controlled to be 11 to 12 using NaOH. After the end of the dropwise addition, the mixture was stirred for a while, and the solution was poured into a 100 ml PVDF reactor and reacted at 150 °C for 15 h. After cooling to room temperature, the resulting precipitate was washed with water and ethanol for several times and dried at 80 °C for 12 h. The powder was dispersed in ethanol and stirred for 12 h, and then dried again at 80 °C for 12 h.

3. Preparation of TFC FO Membrane with or without PNHAs Loading

The PSf substrate was prepared by conventional phase inversion techniques [40]. Generally, PSf, PEG 400, deionized (DI) water, and different amount of PNHAs (0, 0.25 wt%, 0.5 wt%, 0.75 wt%, 1 wt%) were dissolved in DMAc to prepare casting solution (Table 1). The casting solution was cast on a glass plate at room temperature. The blade height was set to 150 μm to quickly wipe a thin film, and then the glass plate was immediately placed in a water coagulation bath for 10 min. After the end, the membrane was placed in a running water bath and rinsed for 24 h to remove residual solvent. The membrane was finally stored in DI water. The substrates were named PSf, PSf 0.25, PSf 0.5, PSf 0.75, PSf 1.0 according to the different PNHAs loading.

The AL was prepared by interfacial polymerization on the prepared substrate [41]. A solution containing 2 wt% MPD, 0.15 wt% SDS was poured onto the dried top surface of the substrate and

Table 1. Synthesis conditions of TFC and TFN FO membranes

Membrane	Support layer					Active layer	
	PSf (wt%)	DMAc (wt%)	PEG400 (wt%)	DI water (wt%)	PNHAs (wt%)	MPD/SDS (water) (wt%)	TMC (hextane) (wt%)
TFC	18.00	73.60	8.00	0.40	0.00	2/0.15	0.1
TFN 0.25					0.25		
TFN 0.5					0.50		
TFN 0.75					0.75		
TFN 1.0					1.00		

soaked for 2 min. The solution was then poured off and the residual droplets were purged with nitrogen. In the next step, the top surface of the substrate was poured into a solution of n-hexane including 0.1 wt% TMC for 1 min. The solution was subsequently poured off and the membrane was heat treated in an oven at 50 °C for 5 min. The membrane was rinsed with water and n-hexane to remove residual solvent and then stored in DI water. The TFC FO membranes were named TFC, TFN 0.25, TFN 0.5, TFN 0.75, TFN 1.0 according to the different PNHAs loading.

4. Characterization of PNHAs and Membrane

Prepared PNHAs were scanned by X-ray diffraction (XRD) in the range of 2θ from 10° to 80°, and the obtained XRD spectrum was compared with a standard spectrum to prove the successful synthesis of PNHAs. The surface morphology of PNHAs was observed by scanning electron microscopy (SEM, JEOL-1600, Japan). The structure of PNHAs was observed by transmission electron microscopy (TEM, JEM-2100, Japan).

All substrate and membrane samples were dried in a 25 °C vacuum oven for 24 h. ATR-FTIR spectroscopy (Thermofisher) was used to analyze the changes of functional groups on PNHAs, PSf and TFN 0.5, and the successful incorporation of PNHAs and synthesis of PA layer in TFC FO membrane were determined. To observe the morphology of substrate and AL, Au film was sprayed by vacuum sputtering coating machine (JFC-1600) for 120 s. The morphology of top surface, bottom surface and cross section of substrate and the top surface of AL were characterized by SEM. To investigate the morphology and surface roughness of the top surface of AL, the top surface of AL was studied by atomic force microscopy (AFM). To research the hydrophilicity of substrate, a drop of DI water was placed on the top surface of the substrate, and then the contact angle was immediately tested by the sessile-drop method, and eight random positions were averaged. To examine the mechanical strength, the substrate was cut into strips of 7 cm×2 cm, and the sample was sandwiched at both ends and stretched at a constant elongation speed of 2 mm/min with a 1 kN load sensor, and the initial length was 2 cm. To obtain the porosity of substrate, dry-wet weighing method was used to measure as shown in Eq. (1) [42]:

$$\varepsilon(\%) = \frac{(m_{wet} - m_{dry})/\rho_w}{(m_{wet} - m_{dry})/\rho_w + m_{dry}/\rho_P} \quad (1)$$

5. Membrane Performance Evaluation

The water permeability coefficient (A) and salt permeability coefficient (B) of membrane were measured by a dead-end filtration cell with an effective membrane area of 28.27 cm^2 and a transmembrane pressure of 1.0 bar at 25±1 °C [43]. To measure A, the top surface of AL or substrate faced the DI water. A was calculated by Eq. (2):

$$A_i = \frac{J_i}{\Delta P}, \; i = T \text{ or } S \quad (2)$$

where J represents the pure water flux ($L/m^2 \cdot h$) which was determined by Eq. (3):

$$J = \frac{\Delta V}{A_m \cdot \Delta t} \quad (3)$$

The water permeability coefficient of AL (A_A) can be calculated by A_T (T means total membrane) and A_S (S means support layer) as shown in Eq. (4):

$$\frac{1}{A_T} = \frac{1}{A_A} + \frac{1}{A_S} \quad (4)$$

To measure B, the top surface of AL or substrate faced with 200 ppm NaCl solution. B was expressed based on the solution-diffusion theory developed by Loeb and Mehta, which was calculated by Eqs. (5) and (6):

$$\frac{1 - R_i}{R_i} = \frac{B_i}{A_i(\Delta P - \Delta\pi)} \quad (5)$$

$$R_i(\%) = \left(1 - \frac{C_p}{C_f}\right) \times 100 \quad (6)$$

B_A was similar to A_A as shown in Eq. (7):

$$\frac{1}{B_T} = \frac{1}{B_A} + \frac{1}{B_S} \quad (7)$$

The water flux (J_w) and reverse salt flux (J_s) of FO membrane were measured by an FO performance evaluation system with an effective membrane area of 10.5 cm^2 at 25±1 °C [44]. During the test, DI water as FS while 1.0 mol/L NaCl solution as DS. FS and DS cycled at a crossflow rate of 330 ml/min on both sides of the membrane. The prepared membrane was analyzed by two different modes: AL-FS (AL facing FS) and AL-DS (AL facing DS), in which the AL-DS mode simulated the permeation performance of TFC membrane in the absence of ICP. J_w ($L/m^2 \cdot h$ (or LMH)) was obtained by measuring the weight changes of DS with digital weight meter, calculation formula just as Eq. (8):

$$J_w = \frac{\Delta V}{A_m \cdot \Delta t} \quad (8)$$

J_s ($g/m^2 \cdot h$ (or gMH)) was determined by measuring the salt concentration changes in FS with conductivity meter, calculation method such as Eq. (9):

$$J_s = \frac{\Delta(C_t V_t)}{A_m \cdot \Delta t} \quad (9)$$

The structural parameter (S) of FO membrane, which can be understood as the necessary distance of solute molecule to permeate through substrate to reach the surface of AL, is a function of substrate thickness (t_s), tortuosity (τ) and porosity (ε). S was calculated by Eq. (10) in the AL-FS mode:

$$S = \frac{D}{J_w} \ln \frac{A_T \pi_{D,b} + B_T}{A_T \pi_{F,m} + J_w + B_T} \quad (10)$$

RESULTS AND DISCUSSION

1. Characterization of PNHAs

Successful synthesis of PNHAs was confirmed by ATR-FTIR spectra and XRD patterns (Fig. 1). As shown in Fig. 1(a), the broad absorption peak at 3,450 cm^{-1} is caused by -OH on the surface of HA, the absorption peak at 1,019 cm^{-1} is a typical PO_4^{3-} group stretching vibration peak, and the absorption peak observed at 601

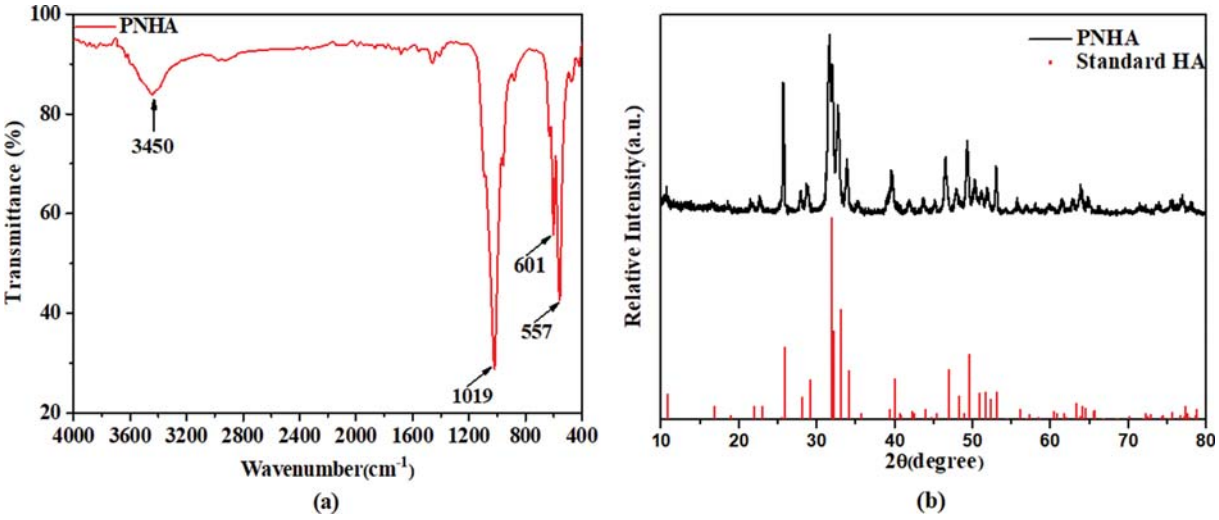

Fig. 1. (a) ATR-FTIR spectra and (b) XRD patterns of PNHAs.

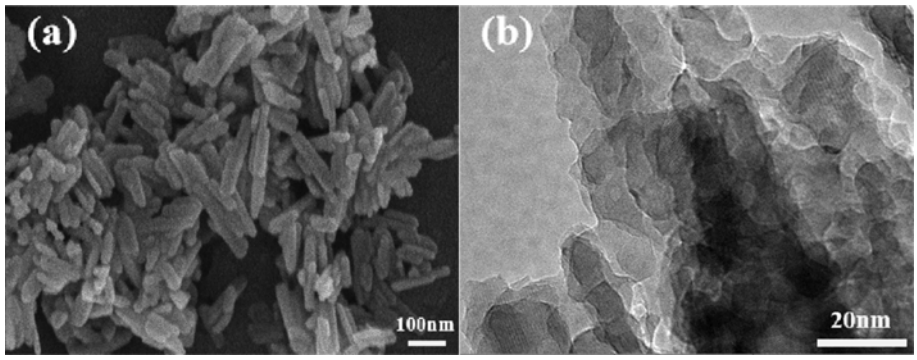

Fig. 2. (a) SEM image and (b) TEM image of PNHAs.

cm^{-1} and 557 cm^{-1} are related to the vibration of O-P-O bond. These characteristic peaks demonstrate the presence of HA. Fig. 1(b) shows the XRD standard pattern of HA (JCPDS 86-0740) and the XRD pattern of prepared PNHAs. As the figure shows, the diffraction peak of PNHAs completely corresponds to the peak of standard HA, indicating that pure hydroxyapatite was successfully prepared and no impurity phase was formed.

To obtain more intuitive morphology and structural information of PNHAs, SEM and TEM analyses were performed on the prepared PNHAs. According to Fig. 2, both SEM and TEM images show that the PNHAs have a rod-like structure with a length of 50 to 150 nm and a diameter of about 20 nm. Due to the high surface charge and surface tension of the nanoparticles under dry conditions, severe aggregation phenomena were observed [45]. The pore structure present on the surface of the PNHAs can be observed in a high-magnification TEM image (Fig. 2(b)). All the above analyses demonstrated the successful synthesis of rod-shaped PNHAs.

The uniform dispersion of nanomaterials in the polymer matrix is a basic requirement for the preparation of composites. As shown in Fig. 3, PNHAs powder was dispersed in the DMAc solution, and after standing for one day, almost no significant precipitation was observed, indicating that PNHAs powder has good dispersibility in the casting solution.

Fig. 3. Photograph of PNHAs dispersed in DMAc solution before (left) and after (right) standing for 1 day.

2. Characterization of Substrate and TFC FO Membrane

The ATR-FTIR spectra of substrate and the TFN 0.5 membrane are shown in Fig. 4. All the samples show significant peaks at wavenumbers of 1,144 cm^{-1} (symmetric O=S=O stretching), 1,298 cm^{-1} (asymmetric O=S=O stretching), 1,237 cm^{-1} (asymmetric C-O-C

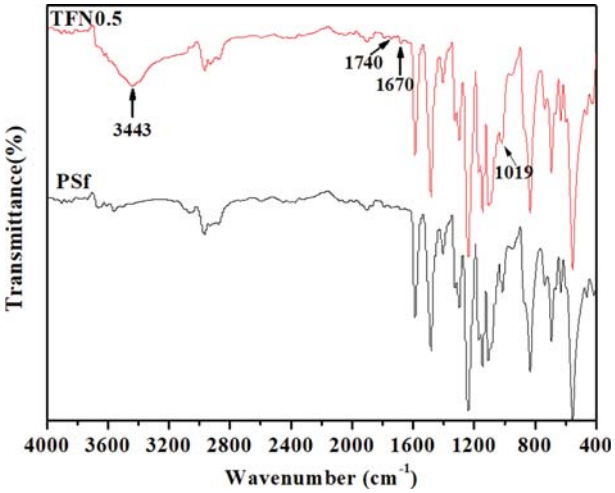

Fig. 4. ATR-FTIR spectra of PSf and TFN 0.5.

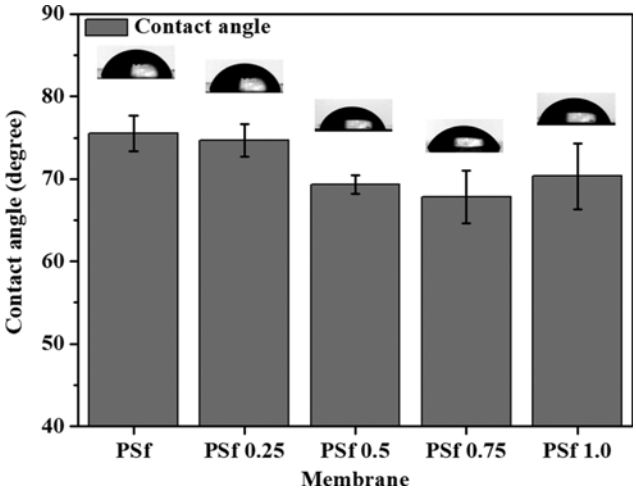

Fig. 5. The water contact angle with different PNHAs loading of the substrate.

stretching), 1,403 cm^{-1} (C=C aromatic ring stretching) and 1,483 cm^{-1} (CH_3-C-CH_3 stretching), which are the characteristic functional groups of PSf polymer. By comparing the spectra of PSf and TFN 0.5, it can be observed that two peaks in TFN 0.5 spectra located at 1,740 cm^{-1} (C=O stretching, amide I band) and 1,670 cm^{-1} (C-N stretching, amide II band) are the specific functional groups of PA structure. These two peaks demonstrate the synthesis of an AL on the PSf substrate. Moreover, the extra peak seen at 1,019 cm^{-1} represents the PO_4^{3-} group, which can prove the successful incorporation of PNHAs in substrate [46].

Fig. 5 is the contact angle (CA) image of the top surface of the substrate. As the PNHAs loading increased, the CA decreased from 75.54° to 67.83° (PSf 0.75). When the loading was increased to 1.0 wt%, the CA increased but was still lower than PSf (70.34°). Analysis of the reasons: although the determination of CA is affected by many factors, the CA is dominated by the chemical properties

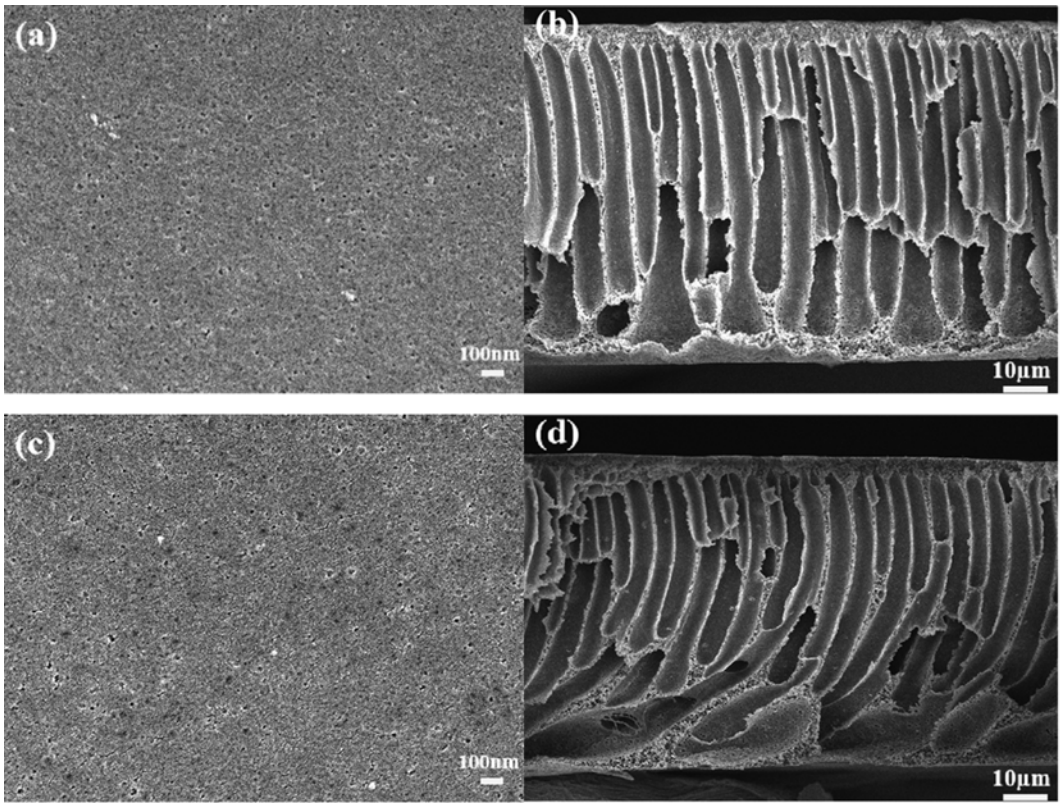

Fig. 6. SEM characterization of substrates prepared with different PNHAs loading: the top surface (left) and cross-section (right) of (a), (b) PSf, (c), (d) PSf 0.25, (e), (f) PSf 0.5, (g), (h) PSf 0.75, (i), (j) PSf 1.0; and the cross section of (k), (l) PSf 1.0 at high magnification.

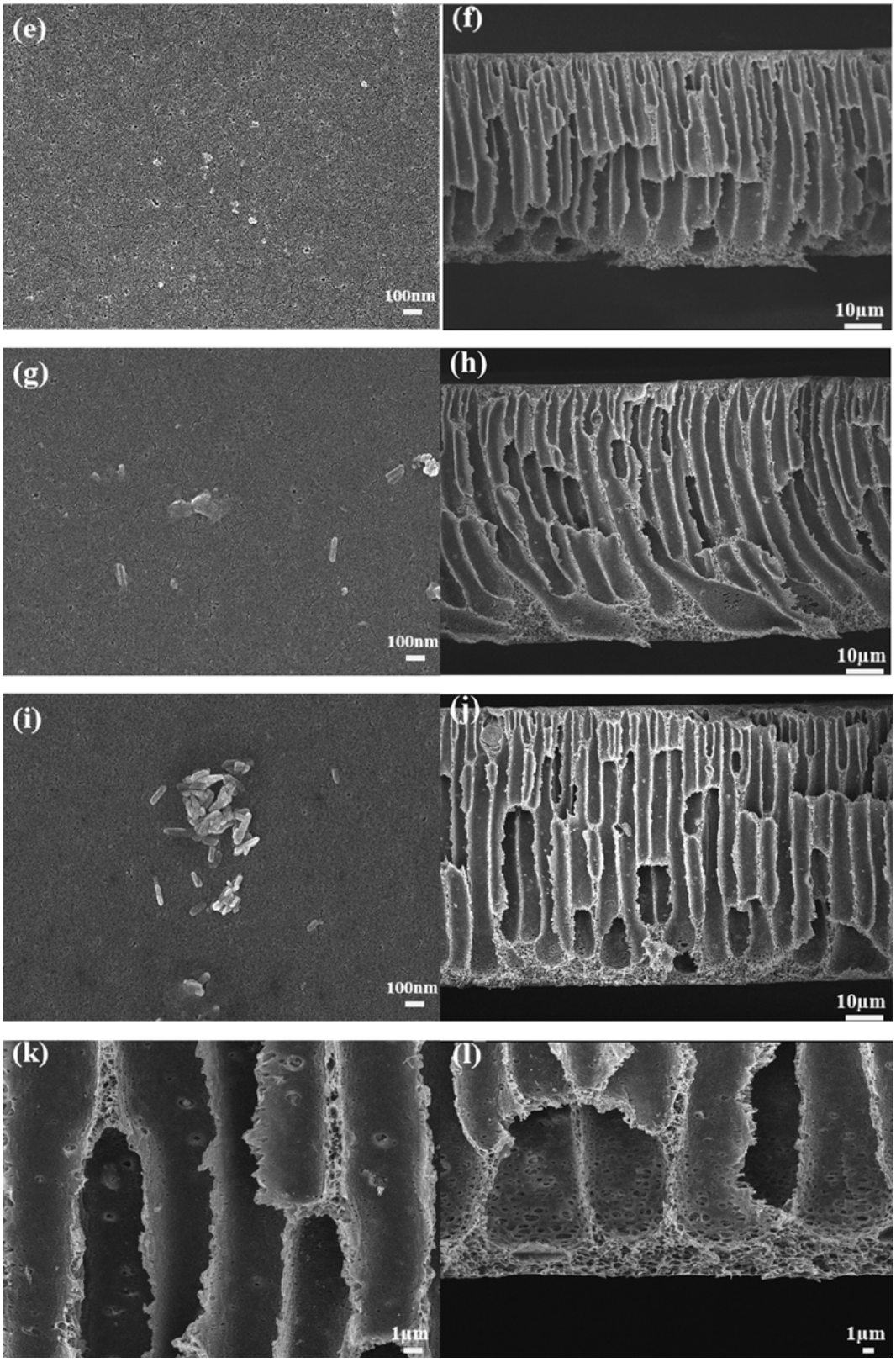

Fig. 6. Continued.

of the material surface. Partially hydrophilic PNHAs concentrate on the top surface of the substrate in order to reduce the surface energy, so as the PNHAs loading increases, the hydrophilicity of the top surface of the substrate increases. When the loading is too

high, the PNHAs agglomeration is severe and the hydrophilicity enhancement effect is weakened [47].

The SEM images of the top surface and cross-section of the fabricated substrates with different PNHAs loading are shown in Fig. 6. It can be observed that all of the substrates consist of a thin sponge-like skin and a long finger-like voids sub-layer, showing a typical asymmetric structure. As PNHAs loading increased, the open pores on the top surface of the substrate decreased and the skin became denser. The thermodynamic mechanism of phase inversion can explain this phenomenon [48]. Since the hydrophobic PSf provided time for the growth of the polymer poor phase, open pores were formed on the top surface of the substrate (Fig. 6(a)). However, the hydrophilic PNHAs in casting solution enhanced the thermodynamic instability, and the non-solvent could rapidly diffuse into the liquid film, hindering the growth of the polymer poor phase, thereby reducing the open pores on the top surface and forming a dense skin (Fig. 6(c)). At the same time, in order to reduce the surface energy, the increasing of PNHAs loading produced more agglomerates. Some PNHAs were exposed on the top surface of the substrate (Fig. 6(e), 6(g)) and even caused some defects (Fig. 6(i)) [49].

Referring to Table 2, as the PNHAs loading increased, the skin thickness decreased from 4.11 μm to 0.75 μm. This is because the presence of hydrophilic PNHAs reduced excessive accumulation of polymer poor phase and avoided the formation of thicker skin.

Table 2. Effect of PNHAs loading on the properties of PSf substrate including porosity (ε), thickness of substrate (l) and skin (l_{skin})

Membrane	ε (%)	l (μm)	l_{skin} (μm)
PSf	70.2±1.0	67.97±0.12	4.11±0.38
PSf 0.25	74.6±0.5	64.60±0.44	3.17±0.09
PSf 0.5	77.1±3.5	56.58±0.92	1.39±0.12
PSf 0.75	80.2±2.4	61.73±0.81	0.90±0.04
PSf 1.0	75.5±2.1	65.17±0.40	0.75±0.07

The skin provided time for the growth of the underlying polymer poor phase, allowing the finger-like pores to develop fully. PSf had the highest thickness (67.97 μm), that is, thick skin led to longer finger-like pores and thicker bottom sponge-like layer.

In addition to being a hydrophilic additive, PNHAs act as nucleating agent to create more pores inside the substrate. The pores created by the uniformly dispersed PNHAs agglomerates loosen the pore walls and provide additional channels for the solute. The additional channels include the pores of the PNHA itself, the pores between the PNHA particles, and the pores between the PNHAs agglomerates and the pore walls (Fig. 6(k)), which greatly increases the connectivity of the channels and provides a straight path for the transport of solute. When the pores are blocked, the solute can select other channels, which also greatly improves the effective porosity [50].

Looking at Fig. 6(b), PSf has a thicker skin and bottom layer, showing a straight finger-like structure, some of which does not extend to the bottom, and the dense and hydrophobic pore wall reduces the channel connectivity; these factors ultimately reduce the effective porosity of substrate. The cross-section images of the PNHAs-loading substrate (Fig. 6(d), 6(f), 6(h)) show the structure of the finger-like pores combined with the macrospores. The skin (from 67.97 μm to 56.58 μm) and the bottom sponge-like layer became thinner. In addition, the uniform dispersion of PNHAs in the pore wall increased the hydrophilicity and connectivity of the pore. The changes of pore structure and chemical property caused by PNHAs loading greatly increased the effective porosity (from 70.2% to 80.2%) of the substrate, shortened the transmission path, enhancing mass transfer, and ultimately alleviating the ICP. Further increasing the PNHAs loading to 1 wt% (Fig. 6(j)), the viscosity of the casting solution was greatly increased, which hindered the phase separation kinetics. At this time, the thickness of the substrate increased (65.17 μm), and the sponge-like pore layer at the bottom became thicker. Severe agglomeration of PNHAs reduced the hydrophilicity of the pore and weakened the mass transfer [51].

The purpose of doping PNHAs is to reduce the S. As men-

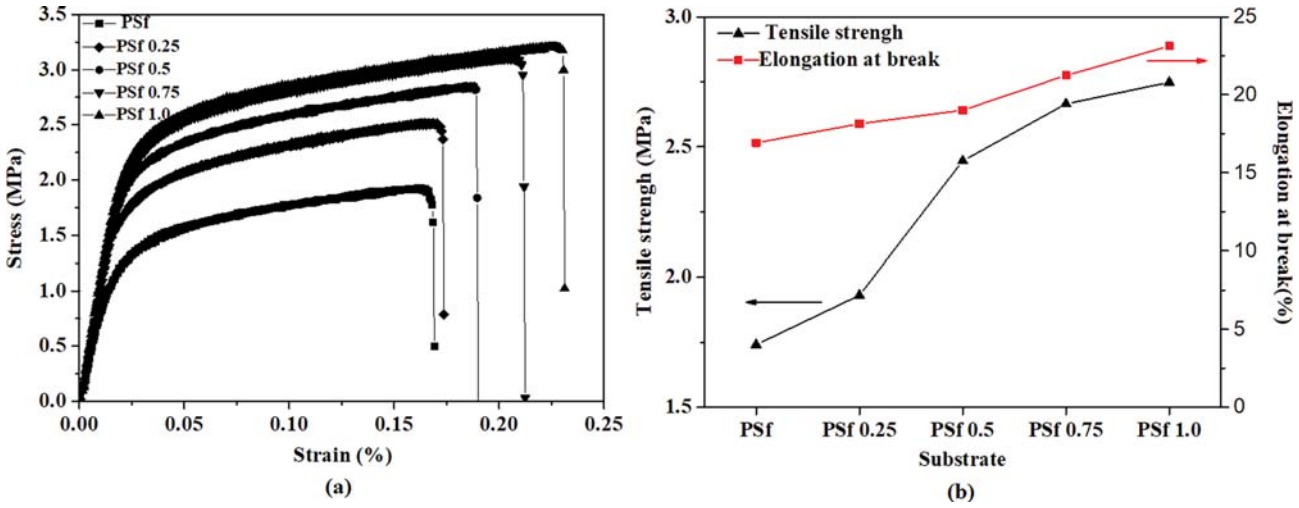

Fig. 7. Mechanical strength characterization of substrates with different PNHAs loading: (a) stress-strain curve, (b) tensile strength and elongation at break.

tioned, appropriate PNHAs loading has a beneficial effect on substrate porosity and thickness. However, as shown in Fig. 6(d) and 6(h), PSf 0.25 and PSf 0.75 show curved finger-like pores. Due to the increased connectivity of the pores, the solute tends to pass through the straight microporous channels. Therefore, tortuosity, especially the tortuosity of PSf 0.75, had a very small effect on S.

Although the FO membrane is used under normal pressure, in order to ensure the normal operation of the membrane under hydraulic conditions, it still needs to reach a certain mechanical strength. Fig. 7 shows the stress-strain curves, tensile strength and elongation at break of different substrates. These properties were enhanced with increasing PNHAs loading. This is due to the strong interfacial interaction between PNHAs and polymer matrix. The external loads can be efficiently transferred to PNHAs with high mechanical strength, so the mechanical strength of the substrate is enhanced. At the same time, the change of pore structure brought by PNHAs loading also enhances the mechanical properties of the substrate.

The modification of the substrate affects not only the structure and properties of the substrate, but also the structure and properties of the PA AL. Fig. 8 shows the top surface SEM images of PA AL prepared on the substrate with different PNHAs loading. The PA layer exhibits a typical ridge-valley surface morphology [15]. The dense surface pores on the substrate hold the MPD solution in the pores, forming a smooth PA layer. However, the open pores on the surface facilitate the migration of MPD solution to TMC solution, resulting in a rough PA layer. Therefore, the top surface of the TFC membrane exhibits a uniform and rough morphology (Fig. 8(a)). With the incorporation of PNHAs, the number of open pores on the surface decreased, and the hydrophilic PNHAs exposed on the surface prevented the diffusion of MPD into the IP reaction area, resulting in many leaf-like structures, and the hydrophilic PNHAs agglomerates promoted the formation of nodular structures (Fig. 8(b), 8(c)). When the PNHAs loading was 1.0 wt%, many large nodular structures were observed (Fig. 8(d)). Leaf-like and nodular structures increased the surface roughness of the membrane, thus increasing the contact area with water. In addition, as the PNHAs loading increased, the surface structure became more and more open, which was beneficial to the improvement of water permeability. Further surface analysis via AFM images can be found in the support information.

3. Intrinsic Separation Properties of TFC FO Membrane

Table 3 shows the water permeability coefficient (A) and salt permeability coefficient (B) for different membranes. A_T was slightly smaller than A_A, and A_S was two-orders of magnitude higher than A_T and A_A. This means that AL plays a major role in the resistance of water molecules and substrate takes second place. With the increase of PNHAs loading, the thickness, porosity (Table 2), hydrophilicity (Fig. 5), and connectivity (Fig. 6) of the substrate improved, so A_S increased from 42.32 (0 wt%) to 69.51 (0.75 wt%) $L/m^2 \cdot h \cdot bar$. Changes in the structure and properties of substrate (Fig. 6) affected the structure of the PA AL, increased the roughness of the PA layer and made the surface more open (Fig. 8), thus affecting the A and raising A_A from 1.86 to 4.14 $L/m^2 \cdot h \cdot bar$, indi-

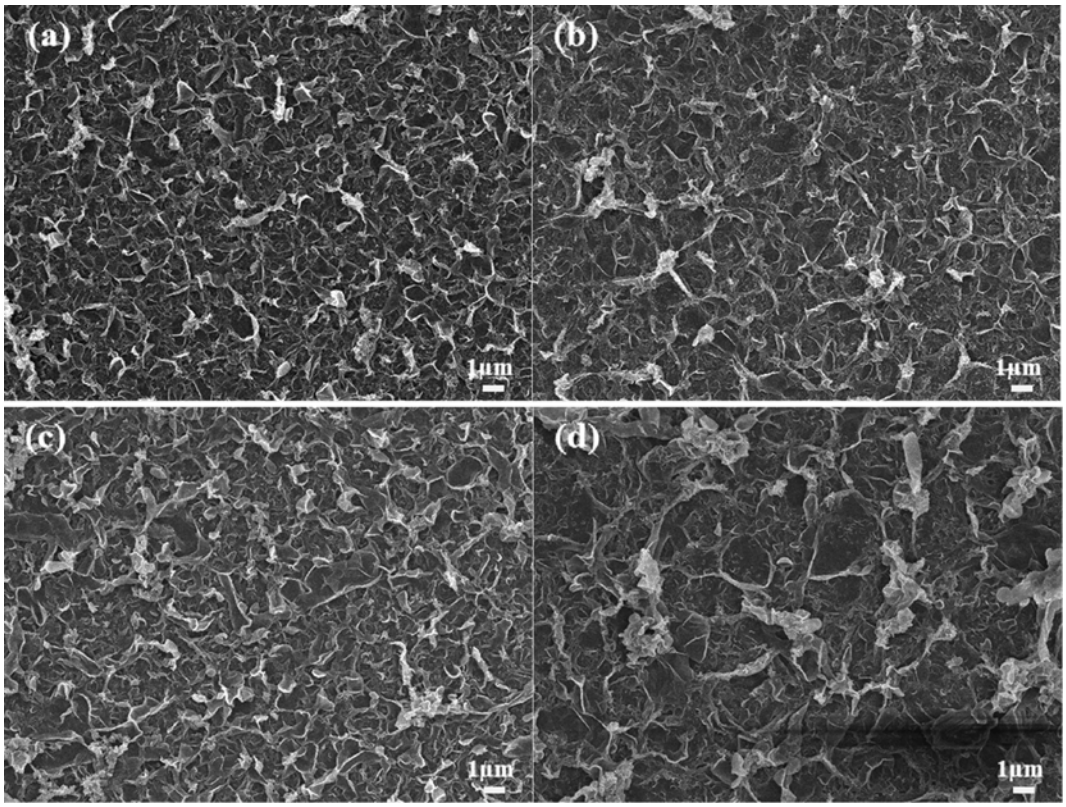

Fig. 8. SEM characterization of active layer on the substrate with different PNHAs loading: top surface of (a) TFC, (b) TFN 0.5, (c) TFN 0.75, (d) TFN 1.0.

Table 3. The permeability coefficient A and B of membrane, support layer and active layer

Membrane	A_T ($L/m^2 \cdot h \cdot bar$)	A_S ($L/m^2 \cdot h \cdot bar$)	A_A ($L/m^2 \cdot h \cdot bar$)	B_T ($L/m^2 \cdot h$)	B_S ($L/m^2 \cdot h$)	B_A ($L/m^2 \cdot h$)
TFC	1.78±0.14	42.32±2.69	1.86±0.15	0.429±0.03	1664.50±105.80	0.429±0.03
TFN 0.25	2.22±0.22	53.78±5.97	2.32±0.23	0.865±0.09	1628.34±85.68	0.866±0.09
TFN 0.5	2.32±0.20	55.96±1.43	2.42±0.23	1.106±0.22	1610.34±50.10	1.107±0.22
TFN 0.75	3.91±0.44	69.51±2.80	4.14±0.52	1.864±0.21	1510.26±85.41	1.867±0.21
TFN 1.0	2.75±0.25	58.37±4.37	2.89±0.27	1.481±0.13	1694.78±153.12	1.482±0.14
HTI-HW	1.19±0.19			0.948±0.05		
HTI-W	0.33±0.04			0.148±0.03		
HTI-NW	0.46±0.07			0.100±0.01		

cating that this rough and open structure was more conducive to water transport. However, when the loading was too high (1.0 wt%), the thickness of substrate and AL increased, the porosity and hydrophilicity of substrate decreased and the A_T decreased to 2.75 $L/m^2 \cdot h \cdot bar$.

B_S was 4-5 orders of magnitude higher than B_T and B_A, indicating that AL determined the mass transfer of salt ions, and substrate could be neglected. The change trend of B_A and B_T was the same as that of A, which showed first an increase and then decrease. It was proved that the influence of PNHAs loading on the structure and properties of SL and AL contributed to the transport of salt ions. When the loading of PNHAs was 1.0 wt%, the B_A was reduced to 1.4819 $L/m^2 \cdot h$, which might have been caused by the increase of PA layer thickness and the decrease of A.

In Table 3 we also list A and B of the flat cellulose triacetate (CTA) FO membrane manufactured by Hydration Technologies Inc. (HTI) [52]. By comparison, the membrane we prepared has a significantly higher A value than the commercial membrane, which sacrifices part of the salt permeability and brings a relatively high B. B/A reflects the selectivity of the membrane. The smaller the B/A, the better the selectivity of the membrane. HTI-NW has the smallest B/A at the cost of extremely low permeability. Compared with HTI-HW and HTI-W membranes, the FO membranes we prepared show better selectivity and higher water permeability, indicating that the membranes we prepared are advantageous.

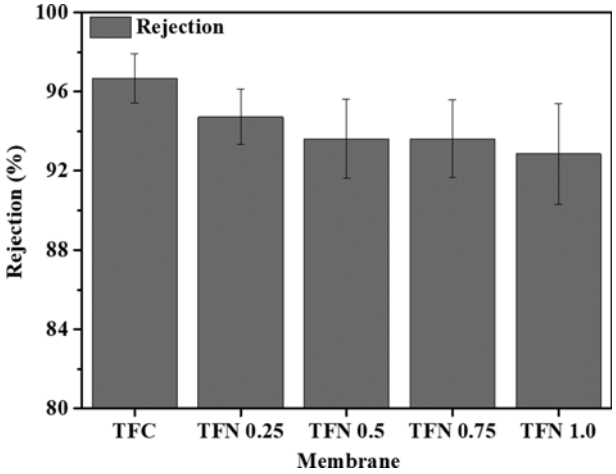

Fig. 9. The salt rejection of the membranes with different PNHAs loadings.

Fig. 9 shows the trend of the salt rejection of the FO membrane with different PNHAs loading in the substrate. With the increase of PNHAs loading, the salt rejection gradually decreased from 96.67% (0 wt%) to 92.84% (1.0 wt%), which was slightly different from the trend of B_T, but more directly showed the impact of structural change to the FO membrane separation performance. In addition, the salt rejection of TFN 0.75 (93.60%) was only slightly lower than that of TFN 0.5 (93.61%). Combined with the analysis in Table 3, TFN 0.75 is the best membrane for water and salt ion mass transfer [28,29].

4. FO Performance Evaluation of TFC FO Membrane

The water flux (J_w) and reverse salt flux (J_s) of the membrane were evaluated by FO experiment, and the results are shown in Fig. 10. Using DI water as FS and 1 or 2 M NaCl as DS, the membranes were tested in AL-FS and AL-DS modes.

As shown in Fig. 10(a), J_w shows a tendency to increase first and then decrease. In AL-FS mode, when 1 M NaCl solution was used as DS, as the PNHAs loading increased, J_w increased from 7.16 (0 wt%) to 18.5 (0.75 wt%) LMH, had an increase of 158%. As discussed earlier (Section 3.2), the loading of PNHAs leads to an improvement in membrane structure and hydrophilicity, which greatly alleviates the ICP and greatly increases the effective osmotic pressure difference, thus increasing the water flux. When the loading of PNHAs was increased to 1.0 wt%, J_w was reduced to 11.93 LMH, indicating that the excessive loading of PNHAs had adversely affected the membrane structure, and the influence of ICP had intensified again; When the NaCl concentration increased to 2 M, J_w of each membrane increased and had the same change trend as when the NaCl solution was 1 M. The TFN 0.75 had the highest J_w (27.6 LMH, improved 178%), but the increase was much smaller than the multiple of the increase of NaCl concentration. This is because the increased DS concentration results in a more severe ICP, and the increase of DS concentration cannot bring about the same increase in effective osmotic pressure difference. This also indicates that it is inefficient to improve the performance of the FO membrane by increasing the concentration of DS, demonstrating that it is feasible to improve the membrane performance by modifying the structure to reduce S; When the membrane was tested in AL-DS mode with 1 M NaCl as DS, J_w showed a different degree of increment compared with AL-FS mode. TFC had

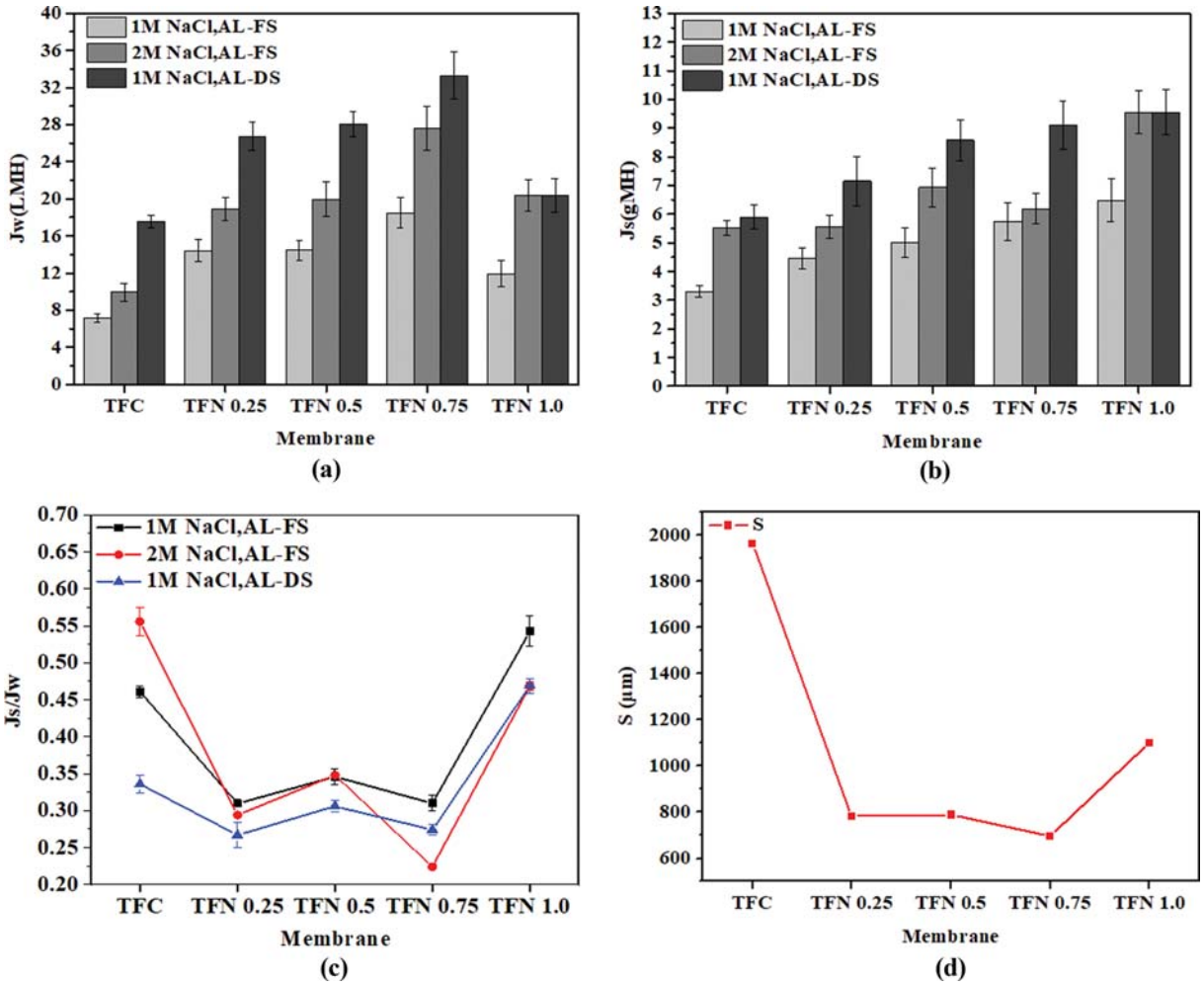

Fig. 10. FO performance of different membranes. (a) water flux (J_w, LMH), (b) reverse salt flux (J_s, gMH), (c) specific reverse salt flux (J_s/J_w) and (d) structural parameter (S). Experimental conditions: 25 °C, DI water as FS and 1 or 2 M NaCl solution as DS, tested at AL-FS and AL-DS mode. M is an abbreviation for the unit mol/L.

the largest improvement (145%), and TFN 0.75 had the smallest improvement (80%). At the same time, TFN 0.75 had the highest J_w (33.26 LMH), only 90% higher than TFC. This is because there is no diluted ICP in AL-DS mode, and the J_w loss caused by the ICP of FO membrane is compensated. PNHAs can enhance the internal mass transfer of the substrate, alleviate the ICP effect. The J_w increment of TFN 0.75 is the smallest, that is, the influence by ICP is the smallest. In the absence of ICP, the PNHAs-loading membrane still exhibits an increased J_w due to factors such as membrane thickness, hydrophilicity, and porosity [30-32].

Fig. 10(b) shows the effect of PNHAs loading on J_s under different modes and DS concentrations. With the increase of PNHAs loading, J_s has a tendency to increase gradually. In AL-FS mode, 1 M NaCl solution was used as the DS. As PNHAs loading increased, J_s increased from 3.3 (0 wt%) to 6.48 (1.0 wt%) gMH. This is related to more open and rough PA layer brought by the PNHAs loading. At the same time, according to the trade-off effect, the increase of J_w is beneficial to the transport of salt ions, resulting in the improvement of J_s. With 2 M NaCl solution as the DS, the J_s was improved due to the increase of the concentration gradient between the FS and the DS. As with J_w, this increase is not multiplied due to the ICP effect. In AL-DS mode, the FO membrane exhibited the highest J_s, because the concentration difference between the FS and the DS is close to the theoretical concentration difference, and the increase of the J_w promotes the transport of the salt ions. Thereby the J_s was greatly increased [33].

J_s/J_w characterizes the selectivity of FO membrane. The smaller the J_s/J_w is, the better is the separation performance of membrane. As shown in Fig. 10(c), the J_s/J_w value ranges from 0.25 to 0.55, indicating that the membrane has good separation performance. As PNHAs loading increased, the J_s/J_w curve under different modes and DS concentrations showed a shape similar to "w". TFN 0.25 had a similar J_s/J_w value to TFN 0.75, but TFN 0.75 has a higher J_w, so 0.75 wt% was the optimal loading for PNHAs.

The structural parameter (S) in Fig. 10(d) represents the length of the path of water molecules through the membrane. The experimental results showed that S decreased from 1,960 μm (0 wt%) to 697 μm (0.75 wt%). When PNHAs loading was further increased, S increased again. It indicated that the structure of TFN 0.75 is most beneficial for mitigating ICP, which corresponds to the previ-

ous statement of changes in membrane structure (Section 3.2) and mass transfer capacity (Section 3.3) brought about by PNHAs loading. The S of the PNHAs-loading membrane was smaller than the TFC FO membrane, which also proved that the influence of PNHAs loading on the FO membrane structure was beneficial to the relief of ICP [36,51].

CONCLUSIONS

The current study added hydrophilic PNHAs powder (ranging from 0 to 1.0 wt%) to the substrate to improve the properties of TFC FO membrane based on PSf substrate. We successfully synthesized rod-like hydrophilic porous nano-hydroxyapatite (PNHAs) with a diameter of about 20 nm and a length of about 100 nm by solvothermal method. The PNHAs incorporated into the substrate were uniformly dispersed in the pore structure and partly agglomerated on the top surface. As the loading of PNHAs was increased to 0.75 wt%, the porosity and hydrophilicity of the substrate were increased, the thickness was reduced, the pore structure was significantly improved, and the mechanical strength was also enhanced. But excessive loading of PNHAs was detrimental to the substrate. The improvement of the structure and properties of the substrate affected the structure and properties of the active layer, and the active layer became more open and rough. For the intrinsic separation properties of the TFC FO membrane, with the increase of PNHAs loading, A increased from 1.78 (0 wt%) to 3.91 (0.75 wt%) $L/m^2 \cdot h \cdot bar$, which is related to the improvement of substrate hydrophilicity and pore structure. At the same time, due to changes in the structure and properties of the active layer, the salt rejection decreased from 96.67% (0 wt%) to 93.60% (0.75 wt%). For the FO performance of the TFC FO membrane, the experimental results showed that the water flux showed an increase from 7.16 (0 wt%) to 18.5 $L/m^2 \cdot h$ (0.75 wt%) in AL-FS mode, and an increase from 17.55 (0 wt%) to 33.26 $L/m^2 \cdot h$ (0.75 wt%) in AL-DS mode, while the reverse salt flux did not increase significantly. When the PNHAs loading increased further, J_w decreased instead. This corresponds to changes in the structure and properties of the substrate. TFN 0.75 had the lowest J_s/J_w (0.31), which means that TFN 0.75 had the highest J_w and the best separation performance. The S of TFN 0.75 was as low as 697 nm, indicating that the incorporation of hydrophilic PNHAs powder into the substrate of TFC FO membrane is an effective strategy to control the ICP effect and enhance the FO performance. The decrease in the S value of the TFN FO membrane substrate is due to higher porosity, enhanced hydrophilicity, and additional water pathways brought about by PNHAs. This paper proves that the incorporation of hydrophilic porous nanomaterials into TFC FO membrane is beneficial to its structure and performance, which will bring great potential to desalination processes such as seawater desalination.

ACKNOWLEDGEMENTS

This work was supported by the National Natural Science Foundation of China (21276132) and the Key Research and Development Program in Shandong Province (public welfare science and technology research project) (2019GSF109038).

NOMENCLATURE

Symbols

A_i : water permeability coefficient, *i* representing total membrane (T) or substrate (S), respectively [$L/m^2 \cdot h \cdot bar$]
A_m : effective membrane area [m^2]
B_i : salt permeability coefficient [$L/m^2 \cdot h$]
C_f : salt concentration of feed solution [mol/L]
C_p : salt concentration of permeated side solution [mol/L]
C_t : salt concentration in feed solution at different times [mol/L]
D : solute diffusion coefficient [m^2/s]
J : pure water flux [$L/m^2 \cdot h$]
J_s : reverse salt flux [$g/m^2 \cdot h$]
J_w : water flux [$L/m^2 \cdot h$]
m_{dry} : weight of dry substrate [g]
m_{wet} : weight of wet substrate [g]
R_i : salt rejection [%]
S : structural parameter [μm]
V_t : volume of feed solution at different times [mol/L]
ε : porosity of substrate [%]
ρ_w : density of water [g/cm^3]
ρ_P : density of PSf [g/cm^3]
$\pi_{D,b}$: bulk osmosis pressure of DS [bar]
$\pi_{F,m}$: osmosis pressure of FS on the FO membrane surface [bar]
ΔP : transmembrane pressure [bar]
ΔV : increment of water permeation volume [L]

SUPPORTING INFORMATION

Additional information as noted in the text. This information is available via the Internet at http://www.springer.com/chemistry/journal/11814.

REFERENCES

1. M. Mulder, *Basic principles of membrane technology*, Kluwer Academic Publications, Netherlands (1996).
2. K. P. Lee, T. C. Arnot and D. Mattia, *J. Membr. Sci.*, **370**, 1 (2011).
3. S. Jiang, Y. Li and B. P. Ladewig, *Sci. Total Environ.*, **595**, 567 (2017).
4. S. Zhao, L. Zhou and C. Y. Tang, *J. Membr. Sci.*, **396**, 1 (2012).
5. S. Lee, C. Boo and M. Elimelech, *J. Membr. Sci.*, **365**, 34 (2010).
6. T. Y. Cath, A. E. Childress and M. Elimelech, *J. Membr. Sci.*, **281**, 70 (2006).
7. D. L. Shaffer, J. R. Werber and H. Jaramillo, *Desalination*, **356**, 271 (2015).
8. S. Lee, C. Boo and M. Elimelech, *J. Membr. Sci.*, **365**, 34 (2010).
9. A. Achilli, T. Y. Cath and E. A. Marchand, *Desalination*, **239**, 10 (2009).
10. R. L. Mcginnis and M. Elimelech, *Desalination*, **207**, 370 (2007).
11. N. Niksefat, M. Jahanshahi and A. Rahimpour, *Desalination*, **343**, 140 (2014).
12. W. Kuang, Z. Liu and G. Kang, *J. Appl. Polym. Sci.*, **31**, 133 (2016).
13. G. T. Gray, J. R. Mccutcheon and M. Elimelech, *Desalination*, **197**, 1 (2006).
14. S. Shokrollahzadeh and S. Tajik, *Desalination*, **425**, 68 (2018).
15. L. Huang and J. R. Mccutcheon, *J. Membr. Sci.*, **483**, 25 (2015).

16. Y. Pan, Q. Zhao and L. Gu, *Desalination*, **421**, 160 (2017).
17. A. K. Ghosh and E. M. V. Hoek, *J. Membr. Sci.*, **336**, 140 (2009).
18. M. J. Park, R. R. Gonzales and A. Abdel-Wahab, *Desalination*, **426**, 50 (2018).
19. X. Chi, P. Zhang and X. Guo, *Appl. Surf. Sci.*, **427**, 1 (2018).
20. S. Lim, M. J. Park and S. Phuntsho, *Polymer*, **110**, 36 (2017).
21. L. Huang, J. T. Arena and J. R. Mccutcheon, *J. Membr. Sci.*, **499**, 352 (2016).
22. S. Sahebi, S. Phuntsho and Y. C. Woo, *Desalination*, **389**, 129 (2016).
23. H. Guo, Z. Yao and J. Wang, *J. Membr. Sci.*, **551**, 234 (2018).
24. H. A. Shawky, S. R. Chae and S. Lin, *Desalination*, **272**, 46 (2011).
25. A. Rahimpour, M. Jahanshahi and A. Mollahosseini, *Desalination*, **285**, 31 (2012).
26. W. Sun, J. Shi and C. Chen, *RSC Adv.*, **8**, 10040 (2018).
27. Y. Wang, R. Ou and Q. Ge, *Desalination*, **330**, 70 (2013).
28. M. J. Park, S. Phuntsho and T. He, *J. Membr. Sci.*, **493**, 496 (2015).
29. J. Yin, E. S. Kim and J. Yang, *J. Membr. Sci.*, **423**, 238 (2012).
30. X. Zhang, L. Shen and C. Guan, *J. Membr. Sci.*, **564**, 328 (2018).
31. W. Kuang, Z. Liu and H. Yu, *J. Membr. Sci.*, **497**, 485 (2016).
32. Y. Wang and T. Xu, *J. Membr. Sci.*, **476**, 330 (2015).
33. M. Ghanbari, D. Emadzadeh and W. J. Lau, *Desalination*, **377**, 152 (2016).
34. A. F. Faria, C. Liu and M. Xie, *J. Membr. Sci.*, **525**, 146 (2017).
35. X. Wu, R. W. Field and J. Wu, *J. Membr. Sci.*, **540**, 251 (2017).
36. Y. Wang, R. Ou and Q. Ge, *Desalination*, **330**, 70 (2013).
37. M. Rastgar, A. Shakeri and A. Bozorg, *Desalination*, **421**, 179 (2017).
38. A. Fihri, C. Len and R. S. Varma, *Coord. Chem. Rev.*, **347**, 48 (2017).
39. Q. Chang, K. K. Li and S. L. Hu, *Mater. Lett.*, **175**, 44 (2016).
40. N. Ma, J. Wei and S. Qi, *J. Membr. Sci.*, **441**, 54 (2013).
41. M. R. Esfahani, S. A. Aktij and Z. Dabaghian, *Sep. Purif. Technol.*, **213**, 465 (2019).
42. S. Morales-Torres, C. M. P. Esteves and J. L. Figueiredo, *J. Membr. Sci.*, **520**, 326 (2016).
43. H. Zuo, J. Fu and G. Cao, *Appl. Surf. Sci.*, **436**, 1181 (2018).
44. J. R. Mccutcheon and M. Elimelech, *AIChE J.*, **53**, 1736 (2007).
45. D. Emadzadeh, W. J. Lau and M. Rahbari-Sisakht, *Chem. Eng. J.*, **281**, 243 (2015).
46. P. Lu, S. Liang and T. Zhou, *RSC Adv.*, **61**, 6 (2016).
47. D. Emadzadeh, W. J. Lau and T. Matsuura, *J. Membr. Sci.*, **449**, 74 (2014).
48. M. L. Yeow, Y. T. Liu and K. Li, *J. Appl. Polym. Sci.*, **92**, 1782 (2004).
49. M. Rastgar, A. Bozorg and A. Shakeri, *Environ. Sci. Technol.*, **52**, 2704 (2018).
50. M. Rastgar, A. Shakeri and A. Bozorg, *Appl. Surf. Sci.*, **441**, 923 (2018).
51. J. R. Mccutcheon, R. L. McGinnis and M. Elimelech, *Desalination*, **174**, 1 (2005).
52. A. Zirehpour, A. Rahimpour and F. Seyedpour, *Desalination*, **371**, 46 (2015).